Simulations of wave–particle interactions in stimulated Raman forward scattering in a magnetized plasma

Pierre Bertrand, A. Ghizzo, S. J Karttunen, T. J H Pättikangas, R. R E Salomaa, M. Shoucri

Simulations of wave–particle interactions in stimulated Raman forward scattering in a magnetized plasma

P. Bertrand, A. Ghizzo, S. J. Karttunen, T. J. H. Pättikangas, R. R. E. Salomaa, and M. Shoucri

Citation: Physics of Fluids B: Plasma Physics **4**, 3590 (1992); doi: 10.1063/1.860368
View online: https://doi.org/10.1063/1.860368
View Table of Contents: http://aip.scitation.org/toc/pfb/4/11
Published by the American Institute of Physics

Simulations of wave–particle interactions in stimulated Raman forward scattering in a magnetized plasma

P. Bertrand and A. Ghizzo
Université de Nancy-I, L.P.M.I.-C.N.R.S. URA 835, B.P. 239, Nancy, France

S. J. Karttunen and T. J. H. Pättikangas
Nuclear Engineering Laboratory, Technical Research Centre of Finland, P.O. Box 208, SF-02151 Espoo, Finland

R. R. E. Salomaa
Department of Technical Physics, Helsinki University of Technology, SF-02150 Espoo, Finland

M. Shoucri
Centre Canadien de Fusion Magnétique, Tokamak de Varennes, IREQ, Varennes, Quebec, Canada

(Received 31 March 1992; accepted 22 July 1992)

Stimulated Raman forward scattering in a high-temperature, magnetized plasma is investigated with relativistic Vlasov–Maxwell simulations and with envelope and test particle calculations. The parameters correspond to Raman current drive by free-electron lasers in reactor grade tokamak plasmas. The phase velocity of the Raman excited plasma wave is large, and therefore the Landau damping is initially weak. The electron plasma wave grows to a large amplitude and accelerates electrons to high energies. Simultaneous pump depletion weakens the driving ponderomotive force, which leads to a collapse of the plasma wave if the number of the interacting electrons is large enough. Spatially the wave–particle interaction takes place in a distance of a few wavelengths of the plasma wave. The electron energies can largely exceed the kinetic energy at the phase velocity of the electron plasma wave. Short-wavelength amplitude modulations of the plasma wave appear at high amplitudes. Efficient generation of the nonresonant anti-Stokes wave and of the second Stokes wave are also observed. Analytical growth rates and envelope calculations explain well the early evolution of the Raman process. Later on, nonlinear wave–particle interactions and relativistic effects start to dominate, and the system is not satisfactorily described by simple envelope equations.

I. INTRODUCTION

The formation of a non-Maxwellian electron distribution with a fast electron tail plays an important role in many fusion applications. In laser fusion, the generation of hot electrons is one of the major problems. Energetic electrons penetrate the pellet core, and the resulting preheating prevents the efficient compression of the fuel. In magnetic fusion, fast electrons are produced in various rf-heating and current drive applications. In noninductive current drive in tokamaks, the fast electrons enhance the current drive efficiency because they are weakly collisional, so that the current is easy to sustain.[1]

Several mechanisms of fast electron generation have been identified during recent years. Usually the mechanisms are based on the presence of large-amplitude electrostatic waves with an appropriate wavelength range. In the case of a single coherent wave, some of the electrons are trapped and accelerated toward the phase velocity of the wave. Fully trapped electrons bounce between two extreme velocities around the phase velocity.

In laser–plasma interactions, fast electrons are produced by the parametric instabilities, such as the two-plasmon decay[2] near the quarter-critical density and the stimulated Raman scattering[3,4] (SRS) below the quarter-critical density. These instabilities generate large-amplitude electron plasma waves with phase velocities $v_{ph} > 2v_e$, i.e., $k\lambda_D < 0.3$, where v_e is the electron thermal velocity, k is the wave number of the plasma wave, and λ_D is the Debye length. If the trapped electrons are accelerated to the phase velocity v_{ph}, their energy is more than ten times larger than the average energy of the bulk electrons.

In stimulated Raman scattering, the scattered electromagnetic radiation may propagate either backward (SRS-B) or forward (SRS-F). The electron plasma wave travels in both cases in the direction of the pump wave. The phase velocity of the plasma wave of SRS-B is very different from that of SRS-F. This difference has a large influence on the energy of the fast electrons. In most practical cases, the Raman backward scattering dominates over SRS-F because SRS-B has a larger gain. At high temperatures and low densities, the plasma wave excited in SRS-B is heavily damped, which implies that the Raman forward scattering prevails in long scale-length plasmas. This type of situation occurs, e.g., in reactor grade tokamak plasmas, where the electron temperature exceeds 10 keV, and in the corona of millimeter-size fusion pellets. The stimulated Raman backward and forward scattering has been extensively studied by particle simulations in unmagnetized plasmas.[5–8]

Stimulated Raman scattering of free-electron-laser (FEL) radiation can be applied to current drive in tokamak plasmas.[9–12] The fast electrons generated by SRS-F are almost collisionless, which improves the current drive

 0899-8213/92/113590-18$04.00

efficiency. In tokamaks, the plasma is magnetized, which has to be taken into account in the simulations of the Raman current drive. The predictions for unmagnetized plasmas are obtained as special cases.

We consider SRS-F in the parameter range, where the phase velocity of the electron plasma wave exceeds $0.9c$. The corresponding energy of the fast electrons is highly relativistic, i.e., $\gamma=(1-v_{\rm ph}^2/c^2)^{-1/2}>2.3$. Our simulations reveal that these plasma waves are, in fact, able to produce even more energetic electrons—in the range $\gamma\approx 4$–12. The presence of a highly relativistic electron tail may improve the current drive efficiency. Vlasov codes suit particularly well for the description of the tail phenomena, where only a small number of electrons is involved. In this type of problem, particle simulation codes suffer from poor statistics.

The dynamics of the wave–particle interaction in SRS is interesting. When the phase velocity of the plasma wave is close to the thermal velocity ($v_{\rm ph}<2v_e$), the heavy Landau damping limits the growth of the plasma wave. This keeps the wave–wave interaction weak, and therefore a very long plasma is required to deplete the pump wave. In the present study, the situation is different because the electron plasma wave has a large phase velocity ($v_{\rm ph}>4.5v_e$). Initially, the Landau damping is negligible, and therefore the amplitude of the plasma wave can reach a high level. This enables a strong interaction of the plasma wave with a fairly large number of electrons. The simultaneous pump depletion and the efficient fast electron generation cause a collapse of the plasma wave. The situation is somewhat similar to the wave breaking, but the present simulations are far from this limit. In current drive, this kind of behavior may be beneficial, because it gives rise to a localized energy transfer from the pump wave to the current carrying electrons.

Another feature of the stimulated Raman forward scattering is a strong, nonresonant generation of anti-Stokes radiation. The anti-Stokes generation reverses the action transfer, and thus it deteriorates the energy conversion from the pump wave to the electron plasma wave. This decreases the current drive efficiency. If the plasma is underdense enough a second Stokes wave can be excited. The energy transfer to the plasma wave is enhanced by the decay of the Stokes wave.

The time scale of our Vlasov–Maxwell simulations is much shorter than the electron collision time. During the simulation we can analyze the microscopic wave–particle dynamics, the tail formation, and the energy transfer from the pump wave to the particles. We are not, however, able to predict the overall current drive efficiency because it depends on the slow collisional relaxation of the tail electrons.

Two-dimensional effects, such as Raman sidescattering and filamentation, are not considered in the present study. The Raman backscattering in an unmagnetized plasma may evolve into the sidescattering as the plasma begins to heat up and the damping for the backscattering increases.[13,14] In a magnetized plasma, the two-dimensional effects may be even more complicated, because the magnetic field makes the nonlinear coupling of the waves anisotropic. Another limitation of the present simulations is that the ions are fixed. This excludes the competition between the stimulated Raman scattering and the processes involving ion modes, e.g., the stimulated Brillouin scattering.[15,16] Furthermore, the fixed ions exclude the modulational instabilities[17] and the coupling of the plasma wave to the ion modes.[18]

The paper is organized as follows. In Sec. II, we describe the basic properties of the stimulated Raman scattering in a magnetized plasma. The simulation parameters and the results of the relativistic Vlasov–Maxwell simulations of the stimulated Raman forward scattering are given in Sec. III. The envelope equations of SRS-F and their numerical solutions are compared with the simulation results in Sec. IV, which also includes a discussion on the anti-Stokes generation. Section V deals with the fast electron generation. Results of the Vlasov–Maxwell simulations are analyzed via simple single-particle calculations, which reveal interesting features in electron acceleration. Finally, the results are summarized in Sec. VI.

II. SRS-F IN A MAGNETIZED PLASMA

Stimulated Raman scattering is the parametric instability in which an intense electromagnetic pump wave $\mathbf{E}_0(\mathbf{k}_0,\omega_0)$ decays into a scattered Stokes wave $\mathbf{E}_-(\mathbf{k}_-,\omega_-)$ and into a longitudinal plasma wave $\mathbf{E}(\mathbf{k},\omega)$: $\mathbf{E}_0\rightarrow\mathbf{E}_-+\mathbf{E}$. Both stimulated Raman backward and forward scattering are possible. In SRS-F, a nonresonant anti-Stokes component may be excited by the coupling between the pump and the plasma wave: $\mathbf{E}_0+\mathbf{E}\rightarrow\mathbf{E}_+$. At very low densities, further cascading of the Stokes and anti-Stokes waves stabilizes the stimulated Raman forward scattering, and the plasma wave can be excited only by the beat-wave method.[19,20]

We study the stimulated Raman forward scattering in such plasma conditions that the backscattering does not occur. We assume a homogeneous plasma and a simple geometry, where all the waves propagate parallel to the external magnetic field $\mathbf{B}_0$. Thus, circularly polarized electromagnetic waves are eigenmodes of propagation. This situation corresponds to the Raman current drive in tokamak plasmas, when the interaction region is located close to the magnetic axis, and the FEL beam is aimed along the field lines.[9,11] In this geometry, the linear dispersion relation of the high-frequency electromagnetic waves reduces to the familiar form,

$$d_j(k_j,\omega_j)\equiv 1-\frac{k_j^2c^2}{\omega_j^2}-\frac{\omega_p^2}{\omega_j^2}\left(1\mp\frac{\Omega_e}{\omega_j}\right)^{-1}=0, \tag{1}$$

where $d_j(k_j,\omega_j)$ is related to the transverse dielectric function, $\Omega_e=|eB_0/m_e|$ is the electron gyrofrequency, $\omega_p=(n_e e^2/\varepsilon_0 m_e)^{1/2}$ is the plasma frequency, and $j=0,-$ stand for the pump and the Stokes wave, respectively. Here, as in the formulas below, the upper sign must be chosen for the right circularly polarized (RCP) waves and the lower sign for the left circularly polarized (LCP) waves. In SRS, the scattered wave has the same polariza-

tion as the pump wave.[9,21,22] The frequency of the pump wave ω_0 is chosen to lie above the cutoff frequency $\omega_{R,L}=[(\Omega_e^2+4\omega_p^2)^{1/2}\pm\Omega_e]/2$. The unmagnetized case is obtained by letting the gyrofrequency go to zero ($\Omega_e\to 0$).

The electron plasma wave, which propagates along the magnetic field $\mathbf{B}_0$, obeys the Bohm–Gross dispersion relation,

$$\epsilon(k,\omega)\equiv 1-\frac{\omega_p^2}{\omega^2}-\frac{3k^2v_e^2}{\omega^2}=0, \tag{2}$$

where $\epsilon(k,\omega)$ is the longitudinal dielectric function and $v_e=(k_B T_e/m_e)^{1/2}$ is the electron thermal velocity. The Bohm–Gross dispersion relation is valid for small values of $k\lambda_D$, where $\lambda_D=(\varepsilon_0 k_B T_e/n_e e^2)^{1/2}$ is the electron Debye length. This is consistent with SRS-F, in which a long-wavelength plasma wave is generated.

The conservation of the energy and momentum determines the phase matching conditions for the Stokes scattering,

$$\omega_-=\omega_0-\omega, \quad k_-=k_0-k, \tag{3}$$

and similarly for the anti-Stokes scattering,

$$\omega_+=\omega_0+\omega, \quad k_+=k_0+k. \tag{4}$$

The phase matching conditions (3) of the Stokes process and the dispersion relations (1) and (2) determine the frequencies and the wave numbers of the waves excited in SRS. Hence, we can calculate the phase velocity of the electron plasma wave, $v_{ph}=\omega/k$, and the quantum efficiency ω/ω_0 of SRS-F, which are important parameters in estimating the efficiency of the Raman current drive.[9,11] The phase velocity of the electron plasma wave characterizes the energy of the fast electrons, and thus their collision frequency. In the current drive, the collisional dissipation must be compensated by the rf power, and therefore it is advantageous to use as fast electrons as possible.

Figure 1 shows the momentum of an electron, which moves at the phase velocity of the plasma wave created by SRS, i.e., $p_{ph}/m_e c=[1-(v_{ph}/c)^2]^{-1/2}v_{ph}/c$. At a temperature of 1 keV, the momentum of a thermal electron with $v=v_e$ is $p_{th}/m_e c=0.044$. At this temperature, we have $p_{ph}/p_{th}=3$–6 in SRS-B and the plasma wave excited by the backscattering is only weakly Landau damped. Therefore SRS-B, which has a larger gain than SRS-F, dominates in this temperature region. In a tokamak reactor, where the electron temperature is 20 keV, we have $p_{th}/m_e c=0.20$. In these conditions, we have $p_{ph}/p_{th}=2$–3 in SRS-B. Hence, the heavy Landau damping suppresses the backscattering and the weakly damped forward scattering can grow much faster than SRS-B. The backscattering is therefore not excited in our simulation.

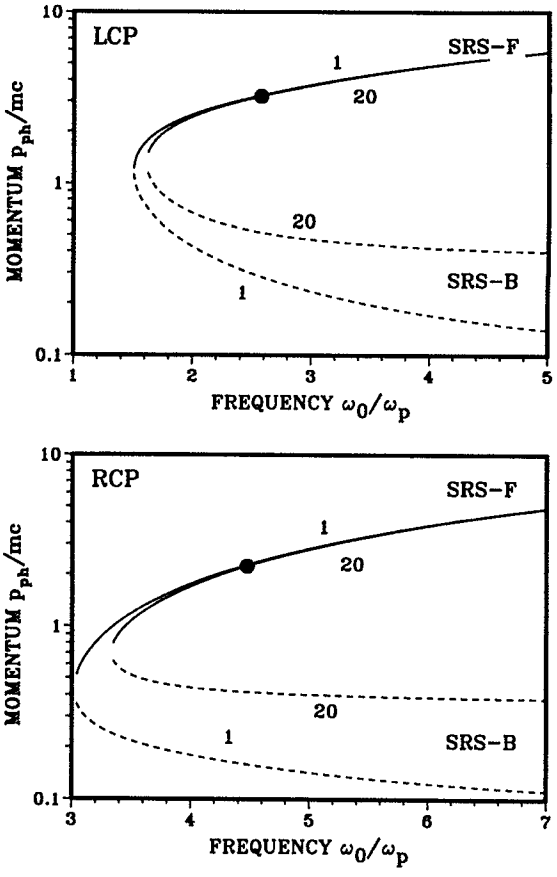

FIG. 1. Momentum of an electron having velocity equal to the phase velocity of the plasma wave, which is created in SRS by a RCP or LCP pump wave with frequency ω_0. The solid line represents SRS-F and the dashed line represents SRS-B at temperatures $T_e=1$ keV and $T_e=20$ keV. The momenta corresponding to the Vlasov simulations are shown by bullets (●).

III. VLASOV–MAXWELL SIMULATION

A. Vlasov–Maxwell code

Most of the simulations to study the beat-wave process or the Raman scattering in a magnetized plasma have been performed by using particle codes (see, e.g., Ref. 9). In this work, we present results obtained from simulations with an Eulerian relativistic Vlasov code. Such a code renders possible the detailed examination of the low-density regions of phase space, which are poorly described in the usual particle in cell (PIC) codes. The code has been successfully applied to study the relativistic electrons produced in the stimulated Raman scattering.[23,24] A second advantage is the noiseless character of the code, which is due to its Eulerian type. This property makes possible a very precise diagnostics of the different fields with the aid of the Fourier and Hilbert analysis,[25] which provide the envelopes and phases of the different modes. Interesting comparisons with the results obtained from envelope equations are then available.

Let us consider plane LCP or RCP waves propagating in the x direction, along the external magnetic field $\mathbf{B}_0$. The plasma can be accurately described by the Vlasov equation for the electron distribution function $F(x,p_x,\mathbf{p}_\perp,t)$:

$$\frac{\partial F}{\partial t}+\frac{p_x}{m_e\gamma}\frac{\partial F}{\partial x}+e\left[E_x+\left(\frac{\mathbf{p}_\perp}{m_e\gamma}\times\mathbf{B}_\perp\right)_x\right]\frac{\partial F}{\partial p_x}+e\left(\mathbf{E}_\perp+\frac{p_x}{m_e\gamma}\mathbf{e}_x\times\mathbf{B}_\perp+\frac{\mathbf{p}_\perp}{m_e\gamma}\times\mathbf{e}_x B_0\right)\cdot\frac{\partial F}{\partial \mathbf{p}_\perp}=0, \tag{5}$$

TABLE I. Free-electron-laser and plasma parameters in the RCP and LCP simulations.

	RCP	LCP
Pump wavelength λ_0 (mm)	0.747	1.29
Electron density n_e (m^{-3})	10^{20}	10^{20}
Electron temperature T_e (keV)	20	20
Magnetic field B_0 (T)	4.81	4.81
Plasma length[a] L (m)	0.181	0.362
Pump intensity I_0 (W/m^2)	3.58×10^{12}	2.28×10^{14}
Relative density n_e/n_{cr}	0.05	0.15
Pump frequency ω_0/ω_p	4.47	2.58
Plasmon frequency ω/ω_p	1.08	1.07
Pump wave number k_0c/ω_p	4.30	2.46
Plasmon wave number kc/ω_p	1.18	1.12
Plasmon phase velocity v_{ph}/v_e	4.61	4.82
Quiver velocity v_0/c	0.027	0.118

[a]Length of the homogeneous plasma.

where $\gamma=[1+(p_x^2+\mathbf{p}_\perp^2)/m_e^2c^2]^{1/2}$. We adopt the Coulomb gauge $\nabla\cdot\mathbf{A}=0$, where the vector potential is in the perpendicular plane. Thus we have $\mathbf{E}=E_x\mathbf{e}_x+\mathbf{E}_\perp$, where

$$E_x=-\frac{\partial\Phi}{\partial x}, \tag{6}$$

$$\mathbf{E}_\perp=-\frac{\partial\mathbf{A}_\perp}{\partial t}. \tag{7}$$

The scalar potential Φ and the vector potential $\mathbf{A}_\perp$ are solved from the Poisson equation and from the Maxwell equations (see, e.g., Refs. 23 and 24 for more details).

The electromagnetic fields $\mathbf{E}_\perp$ are defined as $\mathbf{E}_j=E_{jy}\mathbf{e}_y+E_{jz}\mathbf{e}_z$, where

$$E_{jy}=\tfrac{1}{2}E_j(x,t)\exp[i(k_jx-\omega_jt)]+\text{c.c.}, \tag{8}$$

$$E_{jz}=\pm\tfrac{i}{2}E_j(x,t)\exp[i(k_jx-\omega_jt)]+\text{c.c.} \tag{9}$$

The longitudinal field of the plasma wave is

$$E_x=\tfrac{1}{2}E(x,t)\exp[i(kx-\omega t)]+\text{c.c.} \tag{10}$$

The computational effort for a fully kinetic $1\frac{2}{2}$-D simulation (i.e., four phase space variables x, p_x, p_y, p_z) is enormous. Let us therefore consider the following class of exact solutions of (5):

$$F(x,p_x,\mathbf{p}_\perp,t)=\delta[\mathbf{p}_\perp-\mathbf{P}_\perp(x,t)]f(x,p_x,t). \tag{11}$$

The reduced electron distribution function $f(x,p_x,t)$ describing the particle motion along the x direction satisfies the one-dimensional relativistic Vlasov equation:

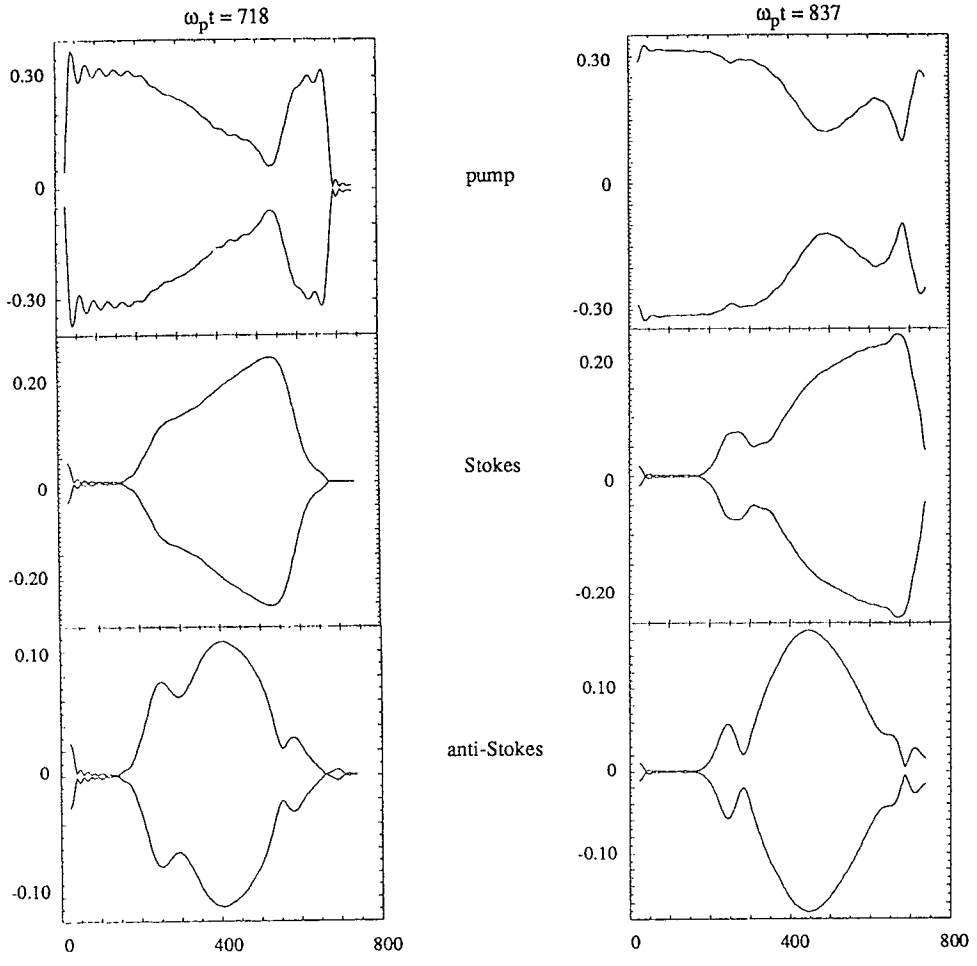

FIG. 2. Spatial dependence ($x\omega_p/c$) of the electromagnetic amplitudes $eE_j/m_ec\omega_p$ at times $\omega_pt=718$ and 837 in the LCP case.

$$\frac{\partial f}{\partial t}+\frac{p_x}{m_e\gamma}\frac{\partial f}{\partial x}+e\left[E_x+\left(\frac{\mathbf{P}_\perp}{m_e\gamma}\times\mathbf{B}_\perp\right)_x\right]\frac{\partial f}{\partial p_x}=0. \quad (12)$$

In this model, the plasma is described by exact "fluid" equations in the direction normal to the external magnetic field, while fully preserving its kinetic features in the direction of the magnetic field. The transverse momentum $\mathbf{P}_\perp$ is obtained through the introduction of the canonical generalized momentum, defined as

$$\mathsf{P}_\perp(x,t)=\mathbf{P}_\perp(x,t)+e\mathbf{A}_\perp(x,t). \quad (13)$$

The momentum $\mathsf{P}_\perp$ satisfies the "fluid" equation

$$\left(\frac{\partial}{\partial t}+u_x\frac{\partial}{\partial x}\right)\mathsf{P}_\perp=\mathsf{P}_\perp\times\mathbf{\Omega}_e-e\mathbf{A}_\perp\times\mathbf{\Omega}_e. \quad (14)$$

It must be stressed that the one-dimensional model is not an approximation but an exact subset of the full kinetic $1\frac{2}{2}$-D Vlasov model. Using periodic boundary conditions a very good agreement has been found between this simplified description and the fully kinetic code both in unmagnetized[26] and magnetized[12] plasmas.

Equations (12)–(14), together with the Maxwell equations for $\mathbf{E}_\perp$, $\mathbf{B}_\perp$, and $\mathbf{A}_\perp$, and with the Poisson equation for E_x, form the basis of our fully relativistic electromagnetic Vlasov code for a magnetized plasma. From a numerical point of view it is convenient to consider the relativistic motion along the x axis only, i.e., to focus the attention to a small population of electrons that have been accelerated to high momenta by the trapping field. In Eq. (12), we have $\gamma=(1+p_x^2/m_e^2c^2)^{1/2}$ as a function of p_x only, which allows the time-splitting scheme with the separation of x and p_x variables to work efficiently on a vector computer like Cray-2.

In this paper, the emphasis is on the development of the Vlasov code for a bounded plasma, which enables us to restore the spatial causality that is destroyed by the periodic boundary conditions. The boundary conditions adopted are very similar to those presented in Ref. 24 for the unmagnetized case.

B. Simulation parameters

We consider a plasma slab of length L surrounded by a void. The plasma is homogeneous except for the steep density gradients at both ends. A circularly polarized pump wave (LCP or RCP) enters the system at one end. All the simulations have been carried out in conditions relevant to the Raman current drive with FEL's in a tokamak reactor: electron density, $n_e=10^{20}$ m^{-3}; magnetic field, $B_0=4.8$ T; and electron temperature, $T_e=20$ keV.

The ratio of the electron cyclotron frequency to the plasma frequency is $\Omega_e/\omega_p=1.5$, which is a typical value on a magnetic axis of a tokamak reactor. The reason for choosing a high electron temperature is that it maximizes the plasma pressure. The high pressure leads to a high bootstrap amplification[27,28] of the FEL-driven seed current, which is necessary to enhance the overall current drive efficiency. The chosen temperature is well in the range where the stimulated Raman forward scattering dominates over the backscattering.[11]

LCP case: As is discussed in Ref. 11, an optimum frequency ratio to maximize the current drive efficiency is $\omega_p^2/\omega_0^2=n_e/n_{cr}=0.15$. With the plasma parameters above, the wave number of the pump wave is $k_0c/\omega_p=2.456$, i.e., the wavelength is $\lambda_0=1.29$ mm. With these parameters, the phase matching conditions (3) for the Raman forward instability predict $\omega_-/\omega_p=1.51$ and $k_-c/\omega_p=1.334$ (Stokes wave) and $\omega/\omega_p=1.07$ and $kc/\omega_p=1.122$ (plasma wave). Typical FEL intensities given in terms of the quiver velocity $v_0=|eE_0/m_e\omega_0|$ in the pump field vary in the range $v_0/c=0.08$–0.118.

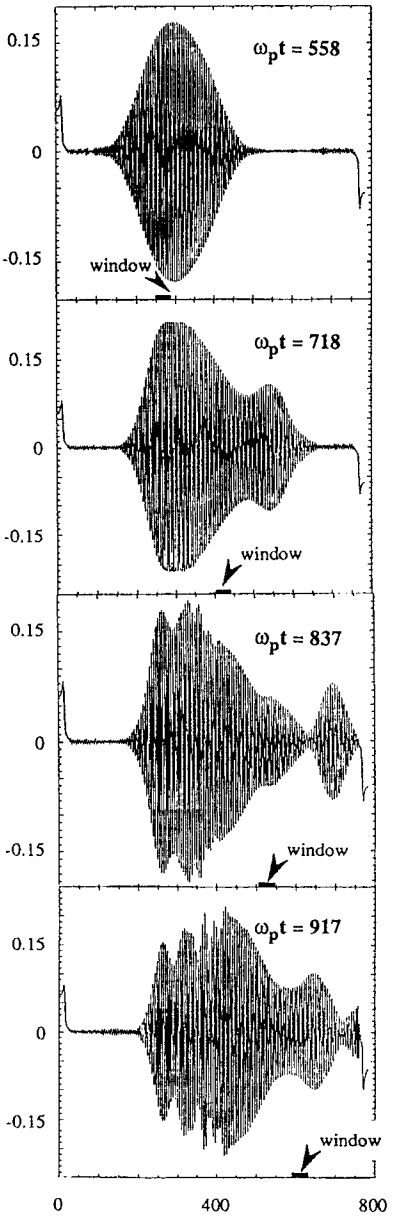

FIG. 3. Spatial dependence ($x\omega_p/c$) of the longitudinal field $eE/m_ec\omega_p$ at various times in the LCP case. The markers show the locations of the moving window of Fig. 12.

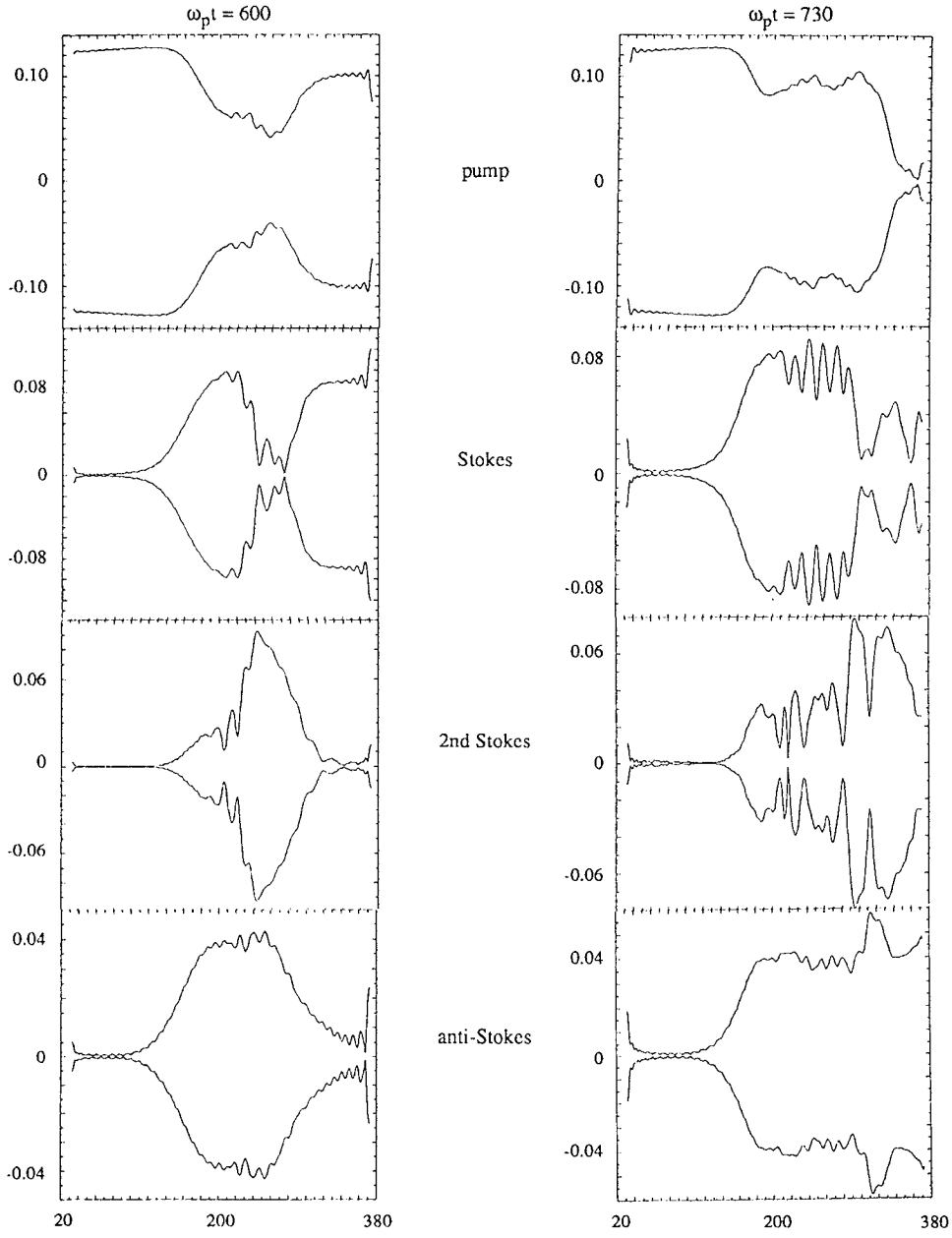

FIG. 4. Spatial dependence ($x\omega_p/c$) of the electromagnetic amplitudes $eE_y/m_e c\omega_p$ at $\omega_p t=600$ and 730 in the RCP case.

An estimate for the basic gain length with $v_0/c=0.08$ is $L_g=15\lambda_0$ (see Ref. 11). To obtain a significant pump depletion, we consider a plasma slab of length $L=280\lambda_0$ or 128λ, where λ is the wavelength of the plasma wave (plus the void and the density jumps on both sides, giving a total length of 140λ). A grid of 4480×1024 mesh points in the (x,p_x) phase space is needed to simulate accurately the system up to $\omega_p t=1000$.

RCP case: An optimum operating point[11] for the current drive is found to be $\omega_p^2/\omega_0^2=n_e/n_{cr}=0.05$ (i.e., $k_0c/\omega_p=4.30$ or $\lambda_0=0.747$ mm) with a laser intensity, corresponding to a quiver velocity $v_0/c=0.027$. The phase matching conditions for the Raman forward scattering now predict $\omega_-/\omega_p=3.393$, $k_-c/\omega_p=3.118$, (Stokes wave) and $\omega/\omega_p=1.079$, $kc/\omega_p=1.183$ (plasma wave). In this case, it was found sufficient to consider a plasma of length $L=64\lambda$ equivalent to $233\lambda_0$. The simulation parameters are summarized in Table I.

The steep density gradient at the entrance of the plasma is sufficient to create a perturbation to start the Raman instability. The ions form a fixed, neutralizing background. In the RCP simulation, the initial electron distribution function is Maxwellian, while in the LCP case a hot tail of 5% 100 keV electrons has been added to enhance the interaction between the plasma wave and the electrons.

C. Raman forward simulations

The envelopes of the different modes of the rapidly oscillating fields can be obtained in a similar way as in the

simulations reported in Ref. 25 for an unmagnetized plasma. At a given time, the signal is Fourier analyzed and thereafter a Hilbert transform is performed, which yields the envelopes of the fields.

Figure 2 shows the Hilbert envelopes of the LCP electromagnetic waves at various times. At an early time $\omega_p t=718$, some pump depletion can be observed. The nonresonant anti-Stokes wave has grown to a level of about one-half the Stokes wave. At later stages, the anti-Stokes mode grows to almost the same level as the Stokes mode. The anti-Stokes generation reverses the energy transfer back to the pump wave so that the pump depletion is not as complete as at earlier times.

The longitudinal electric fields of the LCP case at various times are illustrated in Fig. 3. In the beginning, the plasma wave is well behaved with a smooth envelope. At $\omega_p t=718$, there is a decrease in the amplitude beyond $x\omega_p/c=300$, which is caused by the anti-Stokes generation. Later, at $\omega_p t=837$ and 917, some short wavelength amplitude modulations occur. The modulations appear simultaneously with the fast electron generation, as will be discussed in Sec. V.

The Hilbert envelopes of the electromagnetic waves at different times in the RCP case are displayed in Fig. 4. At $\omega_p t=600$, there is already some pump depletion corresponding to the buildup of the Stokes wave. A clear depletion of the Stokes wave caused by the down-cascading to the second Stokes component can be observed at $x\omega_p/c\geqslant 220$. The amplitude of the second Stokes wave is about the same as that of the primary Stokes wave. Also, an anti-Stokes component appears, but it is somewhat weaker than in the LCP case. Later, at $\omega_p t=730$, the pump depletion is almost complete. In the region of the pump depletion, the Stokes amplitude is considerably reduced due to its further decay down to the second Stokes wave. The down-cascading enhances the action transfer to the plasma waves.

Figure 5 illustrates the longitudinal electric fields in the RCP case. Strong modulations of the envelope are evident. They appear from $\omega_p t=600$ on, and lead, finally, to a collapse of the plasma wave. In Sec. V, we demonstrate that the collapse coincides with strong wave–particle interactions (see Fig. 11).

The wave number spectra of the transverse and of the longitudinal fields in the RCP case are illustrated in Fig. 6 at two instants. At $\omega_p t=600$, the Stokes and the anti-Stokes peaks are clearly resolved in the electromagnetic spectrum. The peaks are in good agreement with the predictions obtained from the phase matching conditions and linear dispersion relations (see Table I). Also, the second Stokes wave can be seen in the electromagnetic spectrum and the corresponding longitudinal spectrum has a side peak at $kc/\omega_p\simeq 1.6$. The phase matching conditions and the linear dispersion relations predict that the wave numbers of the second Stokes wave and of the plasma wave should be $k_{-2}c/\omega_p=1.39$ and $k'c/\omega_p=1.73$, respectively. The peaks in the electromagnetic and in the longitudinal spectra of Fig. 6 match rather well with these values. Later, at $\omega_p t=730$, the side peaks continue to grow and the

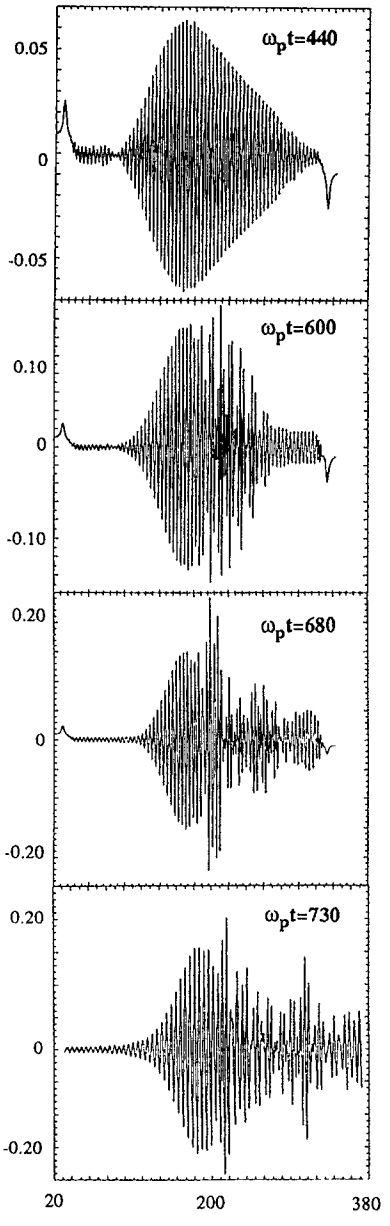

FIG. 5. Spatial dependence ($x\omega_p/c$) of the longitudinal field $eE/m_e c\omega_p$ at various times in the RCP case.

k spectrum of the plasma wave broadens remarkably. The presence of two plasma waves may be responsible for the amplitude modulations appearing in Fig. 5.

The main difference between the performed LCP and RCP simulations is that the Stokes cascading is possible only in the RCP case. The reason for this is that at a temperature of 20 keV the second Stokes scattering of a LCP wave is possible only if $\omega_-/\omega_p>1.60$ (see Fig. 1). Because we had $\omega_-/\omega_p=1.51$ in the LCP simulation, the second Stokes scattering could not occur. The amplitude modulations are stronger in the RCP than in the LCP simulation. The reason for this may be that only in the RCP simulation are there two plasma waves present. Another difference is that in the RCP run the maximum anti-Stokes amplitude remains smaller than in the LCP run.

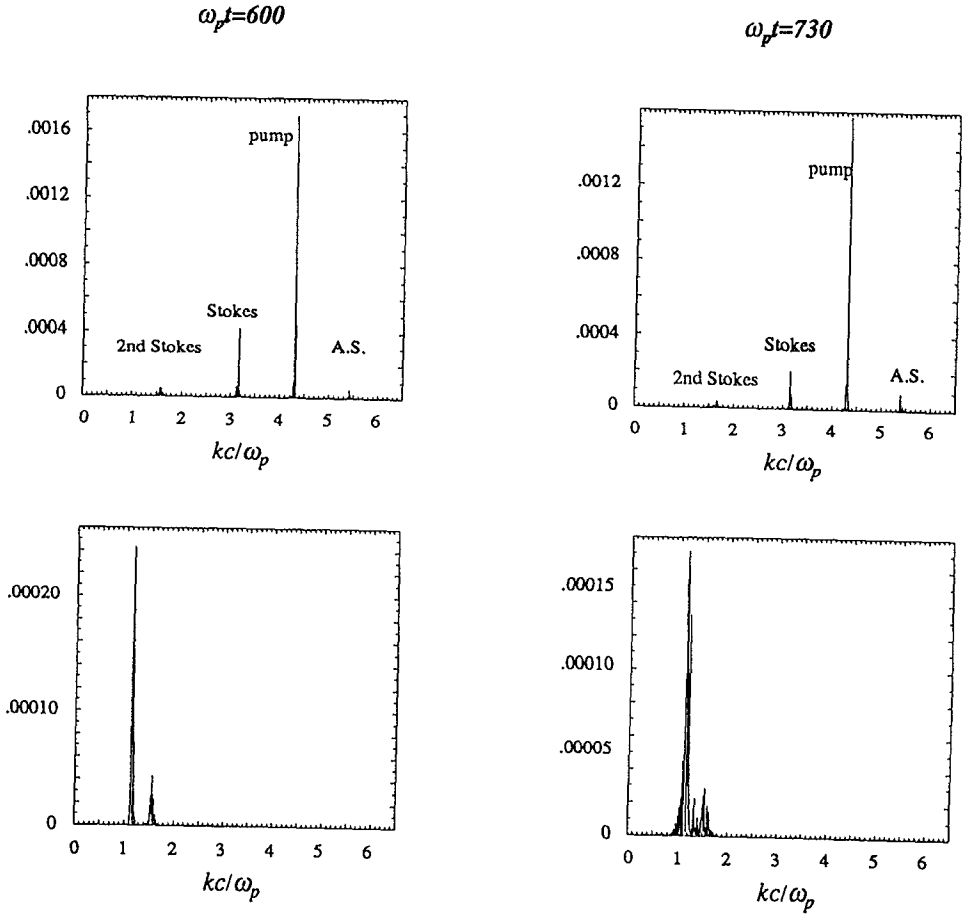

FIG. 6. Wave-number spectrum of the RCP electromagnetic waves (top) at $\omega_p t = 600$ and 730, showing pump, Stokes, second Stokes, and anti-Stokes lines. The lower frames are the spectra of the corresponding plasma waves.

The pump depletion and the action transfer to the plasma waves and fast electrons are therefore more effective in the RCP than in the LCP case. The plasma wave collapse is most likely caused by the wave–particle interactions, which are more important in the RCP than in the LCP simulation.

IV. ENVELOPE MODEL FOR SRS-F

A. Envelope equations

We assume a simplified system in which the electromagnetic field spectrum is composed of the pump, Stokes, and anti-Stokes components, the other components being negligible. The plasma wave has correspondingly only one main Fourier component. Thus the system can be adequately described as a four-wave system. The electric field amplitudes (8)–(10) can be solved from the coupled mode equations for the electromagnetic waves and for the electron plasma wave. The envelope equations can be written as

$$\left(\frac{\partial}{\partial t}+v_{g0}\frac{\partial}{\partial x}+i\delta_0\right)a_0=-K_-a_-a+K_+a_+a^*, \tag{15}$$

$$\left(\frac{\partial}{\partial t}+v_{g-}\frac{\partial}{\partial x}+i\delta_-\right)a_-=K_-a_0a^*, \tag{16}$$

$$\left(\frac{\partial}{\partial t}+v_{g+}\frac{\partial}{\partial x}+i\delta_+\right)a_+=-K_+a_0a, \tag{17}$$

$$\left(\frac{\partial}{\partial t}+v_g\frac{\partial}{\partial x}+\Gamma+i\delta+i\Delta|a|^2\right)a=K_-a_0a_-^*+K_+a_+a_0^*. \tag{18}$$

We have assumed slowly varying amplitudes in time and space for all waves. We have not included the second Stokes wave and the corresponding plasma wave, which start to be important at later stages of the instability. In the RCP case, Eqs. (15)–(18) are therefore able to describe only the early evolution of the system before the secondary Stokes decay sets in. In the following, we apply this model only to the present LCP simulation, where the secondary Stokes scattering is excluded.

The relativistic frequency shift is $\Delta|a|^2$, where

$$\Delta=-\frac{3}{8\varepsilon_0}\left(\frac{\omega}{\omega_p}\right)\left(\frac{e}{m_ec}\right)^2. \tag{19}$$

The relativistic frequency shift is important at high pump intensities when the electron oscillation velocity $v_{osc}=|eE/m_e\omega_p|$ in the field of the plasma wave becomes relativistic.[29] In this case, also the second spatial derivative $i\partial^2 a/\partial x^2$ should be retained in (18) in order to obtain the short-wavelength spatial modulations.

The normalization of the fields is such that the squares of the amplitudes represent the action densities of the waves, i.e., $|a_j|^2=\varepsilon_0|E_j|^2/\omega_j u_j$ and $|a|^2=\varepsilon_0|E|^2/2\omega$. The parameter u_j is defined by

$$u_j=\frac{\omega_j v_{gj}}{k_j c^2}=\left(1\pm\frac{\Omega_e\omega_p^2}{2\omega_j(\omega_j\mp\Omega_e)^2}\right)^{-1}, \tag{20}$$

where the upper and the lower sign refer to the RCP and LCP wave, respectively, and $j=0, +, -$. The plasma wave is considered unmagnetized, i.e., the group velocity is simply $v_g=3v_e^2k/\omega$. Its linear damping rate is denoted by Γ. We have assumed $|\Omega_e\mp\omega_j|\gg k_j v_e$ so that the electron cyclotron damping of the RCP waves is negligible. We have also ignored collisional damping, which is well justified in high-temperature plasmas.

The pump wave $E_0(k_0,\omega_0)$, the Stokes wave $E_-(k_-,\omega_-)$, and the electron plasma wave $E(k,\omega)$ are assumed to be normal modes, i.e., they obey the dispersion relations (1) and (2). Thus we can set in (15), (16), and (18) $\mathrm{Re}\{\delta_0\}=\mathrm{Re}\{\delta_-\}=\mathrm{Re}\{\delta\}=0$, where

$$\delta_0=-\tfrac{1}{2}u_0\omega_0 d_0(k_0,\omega_0), \tag{21}$$

$$\delta_-=-\tfrac{1}{2}u_-\omega_- d_-(k_-,\omega_-), \tag{22}$$

$$\delta=-\tfrac{1}{2}\omega\epsilon(k,\omega). \tag{23}$$

The anti-Stokes wave $E_+(k_+,\omega_+)$ is a quasimode, which means that its wave number k_+ and frequency ω_+ do not satisfy the electromagnetic dispersion relation (1). This gives rise to the mismatch term $i\delta_+$ in (17), where

$$\delta_+=-\tfrac{1}{2}u_+\omega_+ d_+(k_+,\omega_+)\neq 0. \tag{24}$$

Inserting ω_+ and k_+ from the phase matching conditions (4) to the function d_+ in (1), we find

$$\delta_+=-\frac{u_+}{2(\omega_0+\omega)}\left((\omega_0+\omega)^2-(k_0+k)^2c^2-\frac{\omega_p^2(\omega_0+\omega)}{\omega_0+\omega\mp\Omega_e}\right). \tag{25}$$

With the simulation parameters of Table I, we obtain the anti-Stokes mismatch $\delta_+/\omega_p=0.0557$ and 0.0232 in the RCP and LCP case, respectively. The mismatch δ_+ is rather small, even smaller than the thermal correction in the Bohm–Gross dispersion relation, which partly explains the easy onset of the anti-Stokes generation in the simulations.

The coupling coefficients K_+ and K_- in (15)–(18) have been calculated by Sjölund and Stenflo[21] and by Wilhelmsson[22] from the fluid theory of the plasma:

$$K_j=\frac{e}{2m_e}\left(\frac{\omega u_0 u_j}{2\varepsilon_0\omega_0\omega_j}\right)^{1/2}\left|\frac{k_0\omega_j}{\omega_j\mp\Omega_e}-\frac{k_j\omega_0}{\omega_0\mp\Omega_e}\right|, \tag{26}$$

where $j=-, +$ correspond to the Stokes and to the anti-Stokes coupling, respectively.

B. Anti-Stokes generation

In SRS-F, the nonresonant anti-Stokes wave is only weakly detuned, and thus it can grow to large amplitudes in long plasmas. In the following, we shall study in more detail the effects that the anti-Stokes generation has on SRS-F. The second Stokes wave plays a negligible role at the onset of the instability when even the Stokes wave is still very weak. The linear growth rate and the instability threshold can be estimated from the linearized equations for a_-, a_+, and a. Neglecting the pump depletion and the temporal and spatial derivatives, we obtain from Eqs. (16)–(18)

$$i\delta_- a_-=K_- a_0 a^*, \tag{27}$$

$$i\delta_+ a_+=-K_+ a_0 a, \tag{28}$$

$$i\delta a=K_- a_0 a_-^*+K_+ a_+ a_0^*. \tag{29}$$

We find, by eliminating the amplitudes a_- and a_+,

$$\delta\delta_-^*=K_-^2|a_0|^2\left[1+\frac{\delta_-^*}{\delta_+}\left(\frac{K_+}{K_-}\right)^2\right]. \tag{30}$$

We assume complex frequencies $\omega_-=\tilde{\omega}_- -i\Gamma_- +i\gamma$ and $\omega=\tilde{\omega}-i\Gamma+i\gamma$, where $\tilde{\omega}_-$ and $\tilde{\omega}$ are the real parts, γ is the growth rate, and Γ_- and Γ are the damping rates. The real parts of the Stokes and plasma wave frequencies obey the dispersion relations (1) and (2). With the aid of Eqs. (21)–(23) we find $\delta_-^*=i(\gamma-\Gamma_-)$ and $\delta=-i(\gamma-\Gamma)$. Inserting these into Eq. (30), we obtain

$$(\gamma-\Gamma_-)(\gamma-\Gamma)=K_-^2|a_0|^2\left[1+\frac{i(\gamma-\Gamma_-)}{\delta_+}\left(\frac{K_+}{K_-}\right)^2\right]. \tag{31}$$

The growth rate γ and the intensity-dependent frequency shift $\Delta\omega=\mathrm{Re}\{\tilde{\omega}_- -\omega_-\}$ for the stimulated Raman forward scattering can be estimated from

$$\Delta\omega=\frac{K_+^2|a_0|^2}{2\delta_+}, \tag{32}$$

$$\gamma=[K_-^2|a_0|^2-(\Delta\omega)^2]^{1/2}, \tag{33}$$

which are valid well above the threshold ($\gamma\gg\Gamma,\Gamma_-$). The anti-Stokes generation modifies the three-wave process by introducing the frequency shift (32), which increases in proportion to the pump power. This detuning reduces the growth rate from the pure three-wave case, where $\Delta\omega\equiv 0$. The standard three-wave expressions are obtained by letting $\delta_+\to\infty$.

In the present simulations, the frequency shift (32) is small ($\Delta\omega/\omega_p<0.01$), thus having a negligible effect on the growth rate γ. According to Eq. (33), the growth rates with the simulation parameters of Table I are in the LCP (RCP) case $\gamma/\omega_p=0.0140$ (0.0157). The growth rates of the plasma waves in the simulations were determined by measuring the maximum amplitude of the plasma wave at early stages of the instability. The growth rate in the LCP

(RCP) simulation was $\gamma_{sim}/\omega_p=0.009\,14$ (0.0105). This is in rather good agreement with the analytical estimate.

The growth rate (33) reaches its maximum value,

$$\gamma_{max}=\delta_+\left(\frac{K_-}{K_+}\right)^2, \tag{34}$$

at the pump intensity

$$|a_0|^2=2\delta_+^2\left(\frac{K_-}{K_+^2}\right)^2. \tag{35}$$

Above the intensity (35), the frequency shift (32) becomes so large that the growth rate starts to decrease, and γ goes to zero at

$$|a_0|^2=4\delta_+^2\left(\frac{K_-}{K_+^2}\right)^2. \tag{36}$$

In a well-underdense plasma, we have $\omega\ll\omega_0$, so that $\mathrm{Re}\{\delta_+\}$ approaches zero and $\mathrm{Im}\{\omega_+\}$ must be taken into account in (31). This modifies the growth rate (33), which takes the form

$$\gamma=|a_0|(K_-^2-K_+^2)^{1/2}. \tag{37}$$

In the unmagnetized case ($\Omega_e=0$), γ reduces to

$$\gamma\simeq(\omega/2\omega_0)kv_0. \tag{38}$$

This is approximately by the factor $(\omega/2\omega_0)^{1/2}$ smaller than the three-wave growth rate in an unmagnetized plasma, which can be obtained from (33) by setting $\Delta\omega=0$ and $\Omega_e=0$.

In well-underdense plasmas, $\delta_+\to 0$ and a further cascading of the Stokes and anti-Stokes components must be taken into account.[20,30] If $\omega_0\gg\omega$, Ω_e, the dispersion relations of the electromagnetic modes are approximately linear and the phase matching conditions, $\omega_m-\omega_{m-1}=\omega$ and $k_m-k_{m-1}=k$, can be satisfied by several modes. According to Ref. 20 the temporal growth of the electron plasma wave is then no longer exponential, but linear. If there are initially two modes (the pump a_0 and the Stokes wave a_-), the temporal growth of the plasma wave amplitude is given by[20]

$$a(t)\simeq K_-a_0(0)a_-^*(0)t. \tag{39}$$

This follows from the fact that the driving term $\Sigma a_m a_{m-1}^*$ of the electron plasma wave is a constant of motion. If the Stokes wave starts from noise, $|a_-(0)|\ll|a_0(0)|$, the linear growth is very slow according to (39), i.e., the Raman forward scattering is stabilized by the electromagnetic cascading. The plasma wave grows only in the beat-wave method, where the Stokes wave $a_-(0)$ is initially of the same order as $a_0(0)$.

C. Numerical envelope calculations

We have solved Eqs. (15)–(18) numerically in order to test the validity of the envelope model and to obtain more insight into the simulation results. We shall analyze only the LCP case, because the Stokes cascading is not included in our envelope model. The envelope equations were solved by integrating along the characteristics with a simple predictor–corrector method. As an initial condition, we assumed an electrostatic noise level of $e|E(x,0)|/m\omega_p c=0.009$, which is approximately equal to the noise caused by the boundary in the Vlasov simulations. The phenomenological damping Γ in Eq. (18) was assumed to be constant, and it was chosen to obtain an approximate best fit of the envelope calculations to the Vlasov simulation. The goal was to obtain roughly the same depletion length of the pump wave and the same maximum amplitudes of the waves, as in the Vlasov simulation.

The envelopes of the waves in the LCP case at $\omega_p t=658$ are shown in Fig. 7. The maximum amplitudes of the waves obtained from the envelope calculation are close to those obtained from the Vlasov simulation. The phenomenological damping that has been chosen, $\Gamma/\omega_p=0.002$, is not much larger than the linear Landau damping at the plasma conditions of the simulation: $\Gamma_L/\omega_p\simeq 9.0\times10^{-4}$. In this particular case, the plasma length is half of the length used in the rest of the LCP simulations and the pump intensity is $v_0/c=0.12$. The simulation was carried out by starting from a Maxwellian distribution without any hot tail. This reduces the nonlinear wave–particle interactions, which are not included in the envelope model. The agreement between the envelope calculation and the simulation is excellent, which indicates that the nonlinear wave–particle interactions are negligible at this time.

Envelopes of the waves in the LCP case at $\omega_p t=718$ are shown in Fig. 8. The simulation is similar to the one shown in Figs. 2 and 3, except that no fast electron tail was introduced. The phenomenological damping, which has been chosen in order to obtain the best fit, is $\Gamma/\omega_p=5\times10^{-3}$. This exceeds the linear Landau damping $\Gamma_L/\omega_p\simeq 4.0\times10^{-4}$ by more than an order of magnitude. A heavy phenomenological damping is needed, because the wave–particle interactions affect strongly the plasma wave at $\omega_p t=718$. The same damping coefficient gives a rather good fit to the simulation results also at an earlier time, $\omega_p t=598$.

The maximum amplitudes of the waves obtained from the envelope calculation are roughly equal to those obtained from the Vlasov simulation (see Fig. 8). There are, however, some distinct differences. The depletion length of the pump wave is shorter than in the Vlasov simulation, even though the damping in the envelope calculation is much larger than the linear Landau damping. Another difference between the Vlasov and the envelope calculation can be seen in the shape of the envelope of the plasma wave. This difference is mainly caused by the wave–particle interactions that occur in the Vlasov simulation. The envelopes of the Stokes and of the anti-Stokes waves agree quite well with those obtained from the Vlasov simulation.

The importance of the relativistic and linear detuning in Eq. (18) was studied by repeating the envelope calculation with $\Delta=0$ and with $\delta_+=0$, respectively. As expected, the effect of the relativistic detuning on the waves is largest near the maximum of the plasma wave (see Fig. 8). In regions where the amplitude of the plasma wave is small

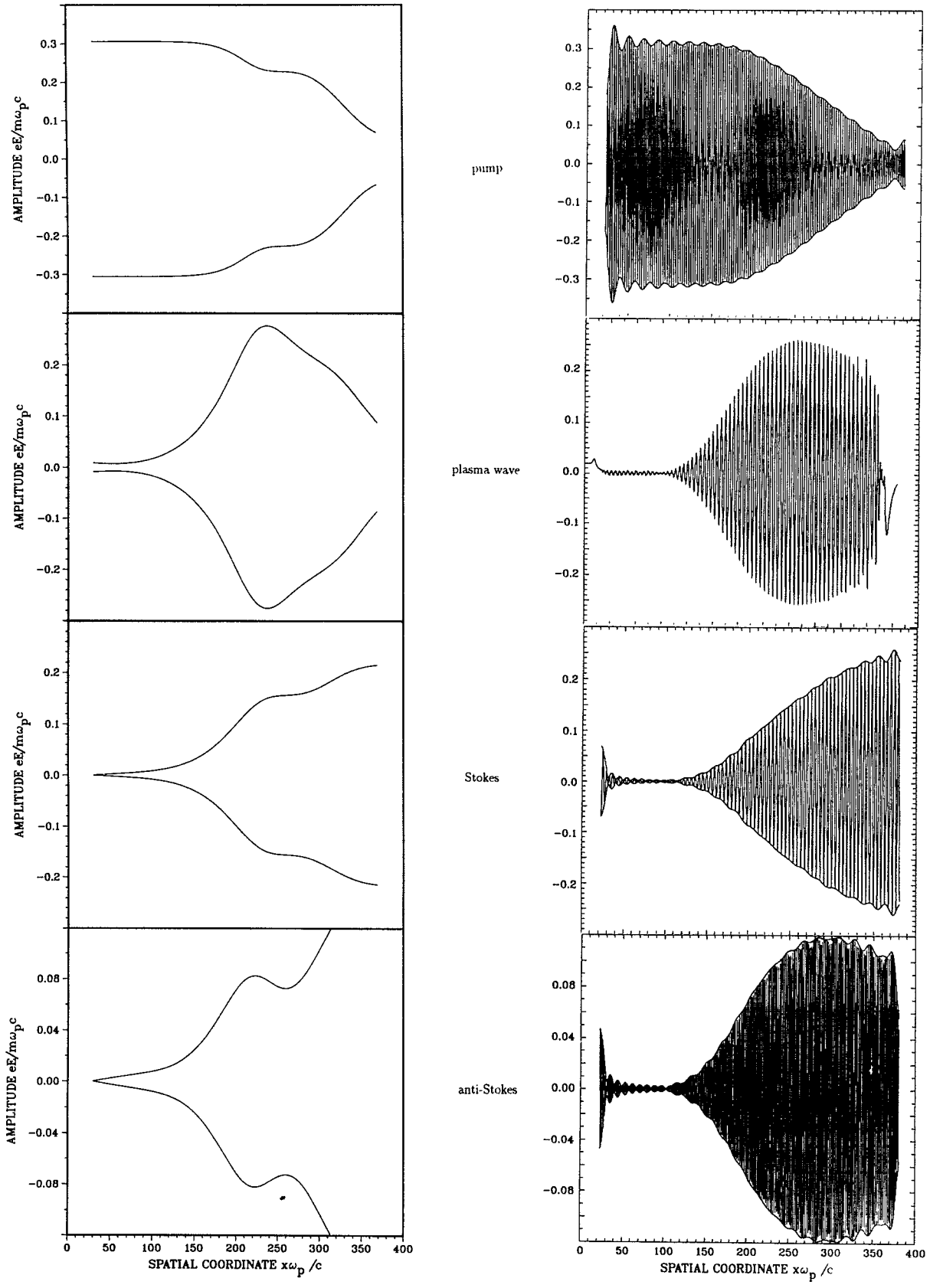

FIG. 7. Envelopes of the waves in the LCP case for a short plasma ($L\omega_p/c=358$) at time $\omega_p t=658$. Envelopes obtained from the envelope code are shown on the left and the results obtained from the Vlasov code by the Hilbert transform are shown on the right ($\Gamma=0.002\omega_p$).

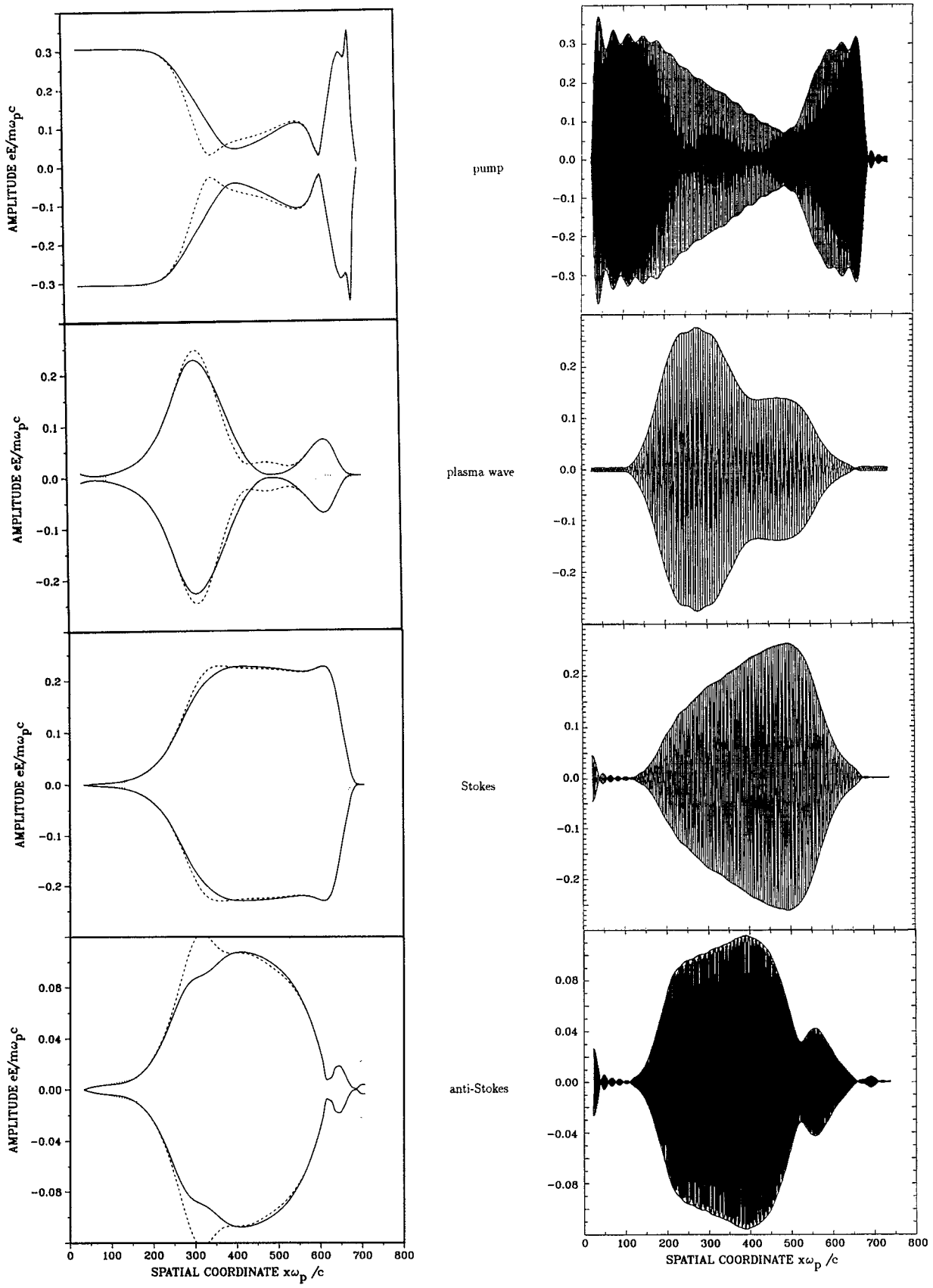

FIG. 8. As in Fig. 7, but for the LCP case in a long plasma at time $\omega_p t=718$, assuming $\Gamma/\omega_p=0.005$. Solid line represents the best fit obtained from the envelope calculations. Dashed and dotted lines are used for the results obtained without the relativistic detuning ($\Delta=0$) and without the linear detuning ($\delta_+=0$), respectively.

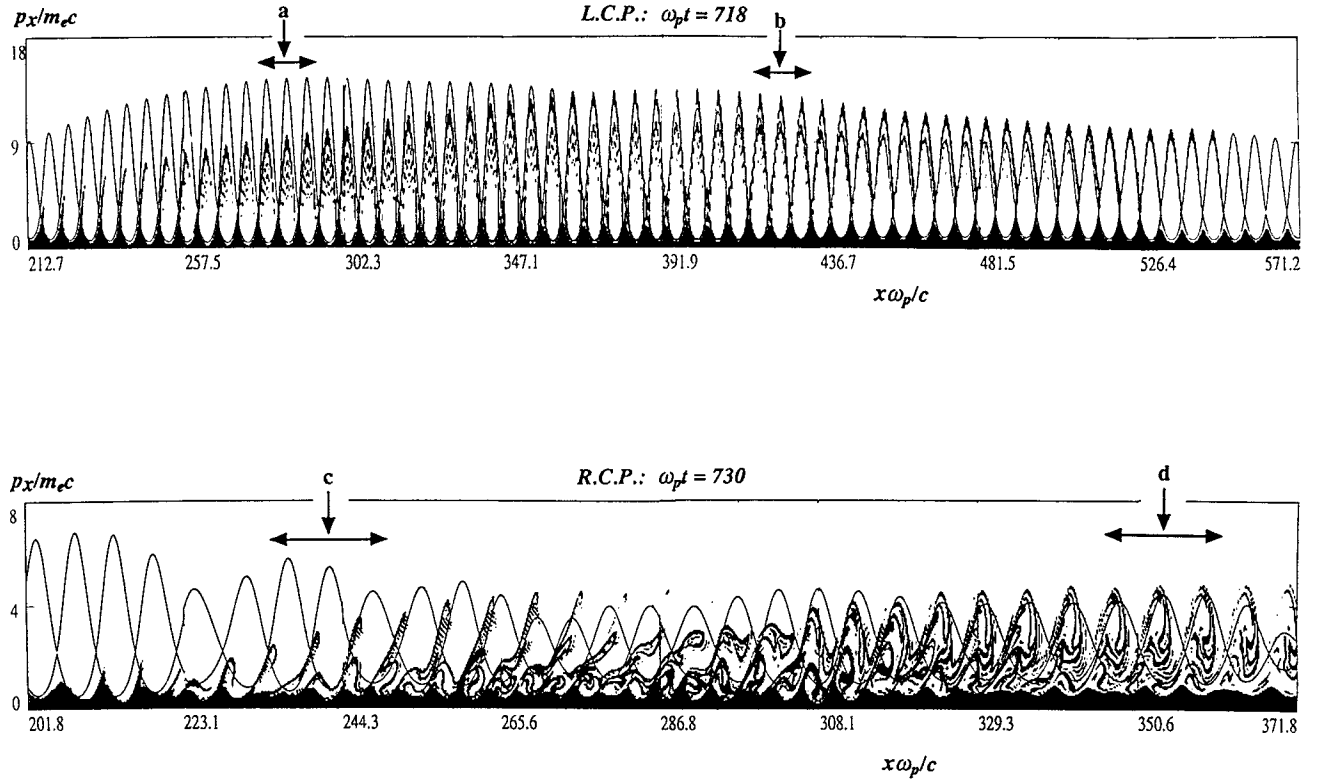

FIG. 9. Phase space (p_x,x) at $\omega_p t=718$ (LCP) and at $\omega_p t=730$ (RCP). The solid line corresponds to the separatrix momentum of the marginally trapped electrons. Notice the different momentum scales. The markers a–d refer to the electron velocity distributions of Fig. 10.

$(e|E|/m\omega_p c<0.1)$ the relativistic detuning is insignificant.

The envelope calculations show that the stimulated Raman scattering is rather sensitive to the amount of the linear detuning δ_+ (see Fig. 8). When we have $\delta_+=0$ the anti-Stokes wave is resonant and already grows at the beginning of the interaction. This tends to stabilize the Raman process by reversing the action transfer. Since the action is transferred from the plasma wave to the anti-Stokes wave, the amplitude of the plasma wave remains low and the anti-Stokes wave becomes large. On the other hand, the Stokes wave remains small because it is driven by the weak plasma wave.

The main reason for the differences between the envelope calculations and the Vlasov simulations is the very simple model for the plasma wave damping. The nonlinear wave–particle interactions that depend on the amplitude of the plasma wave cannot be modeled by linear damping that is constant in time and space. Even damping that depends on the amplitude of the plasma wave, e.g., $\Gamma=\Gamma_L+\Gamma_{NL}|a|^2$, does not give good results. This kind of instantaneous nonlinear damping decreases drastically the maximum amplitude of the plasma wave and gives results that are in strong contradiction with the Vlasov simulations.

In conclusion, the slowly varying envelope equations describe the early evolution of the waves fairly accurately, and they apply particularly well to weakly driven systems. At modest amplitude levels, the use of an effective linear damping gives reasonable results, and the envelope model is useful in applications that are cumbersome to describe by Vlasov simulations. In the strongly nonlinear regime, the wave–particle interactions are important, which makes the envelope approach very difficult. In this case, the Vlasov or the particle simulations are the most reliable methods if accurate results are needed.

V. GENERATION OF ULTRAFAST ELECTRONS

In Ref. 24, we have shown that our Vlasov code is able to give a precise description of the phase space dynamics. The correlation with the simple orbit theory is striking even when the waves are not steady, so that separatrices, strictly speaking, do not really exist. We recall that the separatrix momentum can be easily calculated from the potential obtained from the output data of the code by using Eq. (23) of Ref. 24. Figure 9 shows a portion of the phase space plots at a fixed time for the RCP and LCP polarizations. The grey shade indicates the magnitude of the particle distribution function $f(x,p_x)$. The solid curves mark the separatrix between the trapped and untrapped particle orbits for the local amplitude of the plasma wave. More details of the particle distribution functions can be found in Fig. 10, which displays $\langle f(x,p_x)\rangle$ at various central positions x. The spatial average $\langle f(x,p_x)\rangle$ is over three wavelengths of the plasma wave. In Fig. 10, the momentum scale is replaced by the kinetic energy $\gamma-1$.

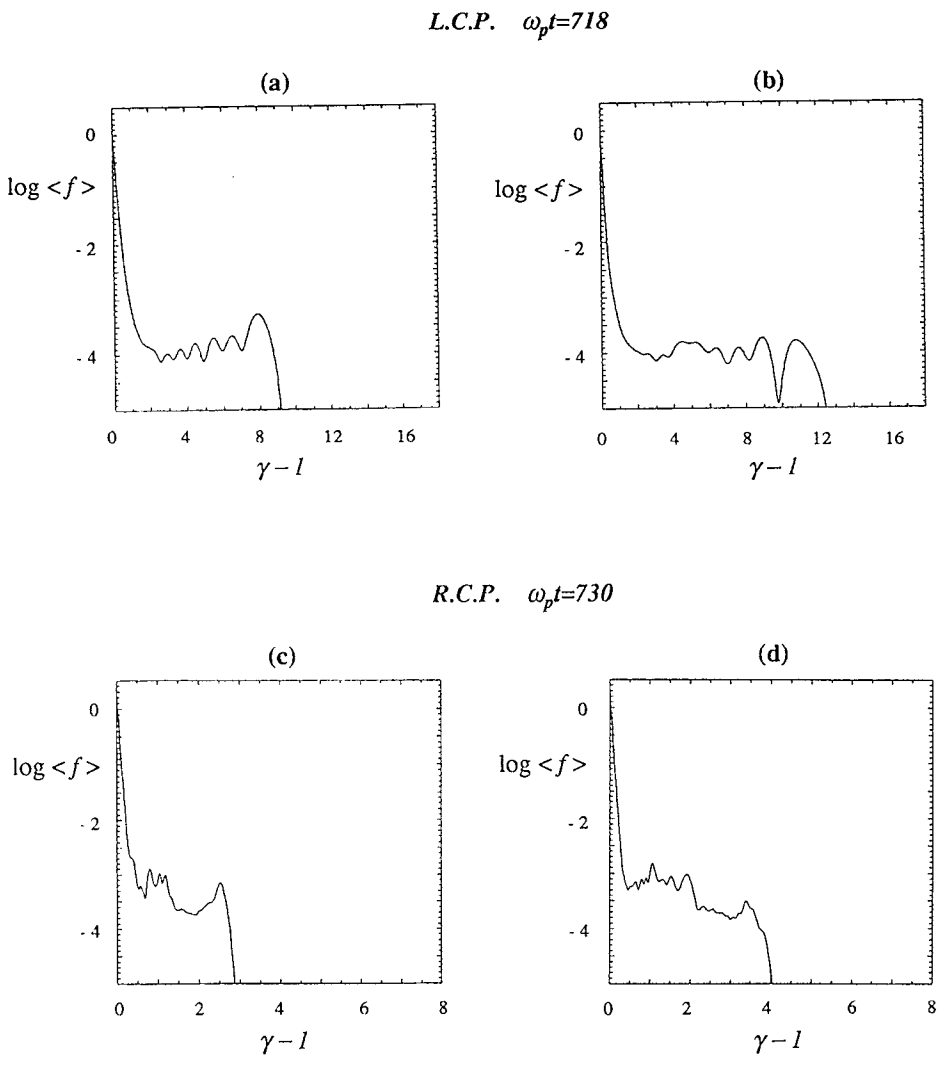

FIG. 10. Electron velocity distributions $\langle f(x,p_x)\rangle$ as a function of $\gamma-1$ at $\omega_p t=718$ (LCP) and at $\omega_p t=730$ (RCP) around the central positions marked in Fig. 9. The spatial average $\langle\ \rangle$ is over three wavelengths of the plasma wave.

The simulations demonstrate the generation of ultrafast electrons with $\gamma>4$ corresponding to total energies that exceed 2 MeV. The phase velocity of the electron plasma wave in the RCP case, $v_{\rm ph}=\omega/k=0.912c$, would suggest a considerably smaller electron energy $\gamma=2.44$. The plateau in the distribution function settles at a level of about 10^{-3} of the peak value in the RCP simulation. In the LCP simulation, the phase velocity of the plasma wave, $v_{\rm ph}/c=0.955$, is larger than in the RCP simulation, and therefore the plateau is low, even though a hot tail with 100 keV electrons was added to the initial distribution. In the RCP run, the overall local hot electron density is thus of the order of 10^{-3} of the bulk density. It is also worth noticing the stratified structure of the hot electron tail of the distribution function (see Fig. 10). The wave–particle interaction is stronger and more chaotic in the RCP simulation due to the larger number of the fast electrons. Also, the second plasma wave created by the second Stokes scattering in the RCP run increases the wave–particle interaction, because its phase velocity is only $v_{\rm ph}=0.67c$. A sign of the second plasma wave can be seen in the distribution function of Fig. 10(c) at $\gamma-1=0.35$. The phase space plot of the LCP run is much more regular and adiabatic, even though there is initially a hot tail to enhance the wave–particle interaction. In the momentum space, the LCP tail extends to much higher values (up to $\gamma-1=12$).

The wave–particle interaction is very strong in the RCP simulation, in spite of the large phase velocity of the plasma wave, $v_{\rm ph}/v_e=4.61$ (see Fig. 9). The reason for this is that the plasma wave instantaneously reaches such a high local amplitude that the number of the electrons within the trapping region becomes non-negligible. Because the lower trapping velocity has to be close to v_e before there is any appreciable number of interacting electrons available, the plasmon may first grow almost undamped to a large amplitude. After the overshoot the plasmon quickly collapses with the onset of an efficient energy transfer to the accelerated electrons. This sequential behavior occurs, especially in the RCP simulation, and can be seen in Fig. 9, where the magnitude of the local plasma wave amplitude can be deduced from the width of the separatrices.

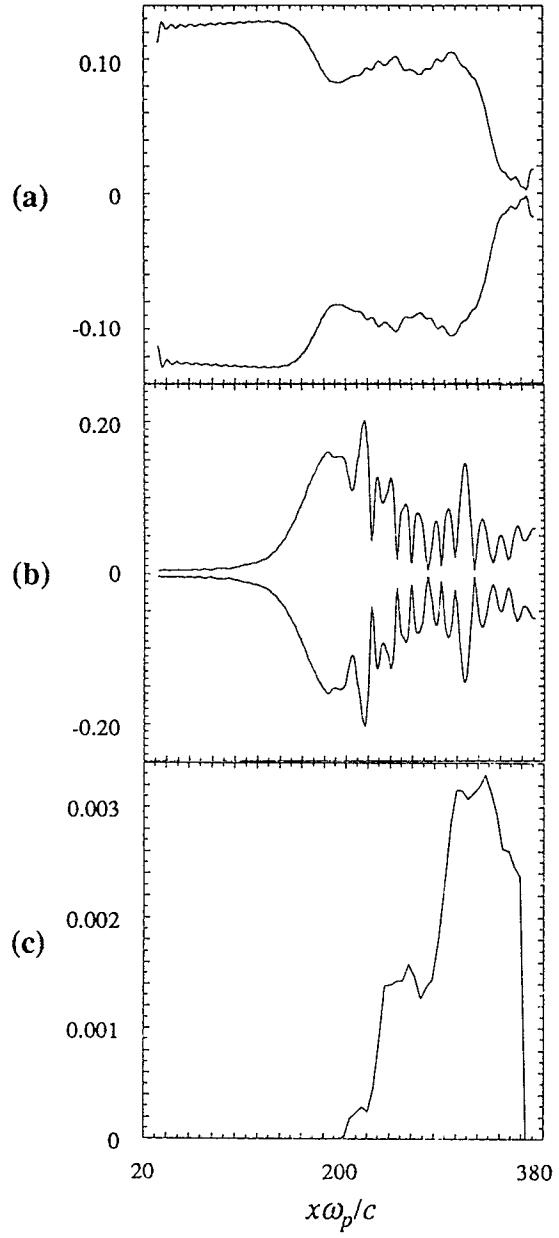

FIG. 11. The electric fields of the (a) pump wave and (b) electron plasma wave, and (c) the action density of the fast electrons at $\omega_p t=730$ in the RCP case. Note the sequential action transfer: pump→plasma wave→electrons.

The rather complete pump depletion is evident from the simulations. Figure 11 displays the amplitude of the RCP pump wave and of the electron plasma wave and the action density of the hot electrons defined by

$$N_e=\frac{1}{\omega_p}\int_{p_{\rm low}}^{\infty}(\gamma-1)f(x,p_x)dp_x\,, \tag{40}$$

where $p_{\rm low}=p_{\rm low}(x)$ is the value of the momentum p_x corresponding to the lower branch of the separatrix. The action transfer to the electrons leads to an almost complete local depletion of the plasma wave. As the pump is emptied in the same region, there is no chance for the plasmon

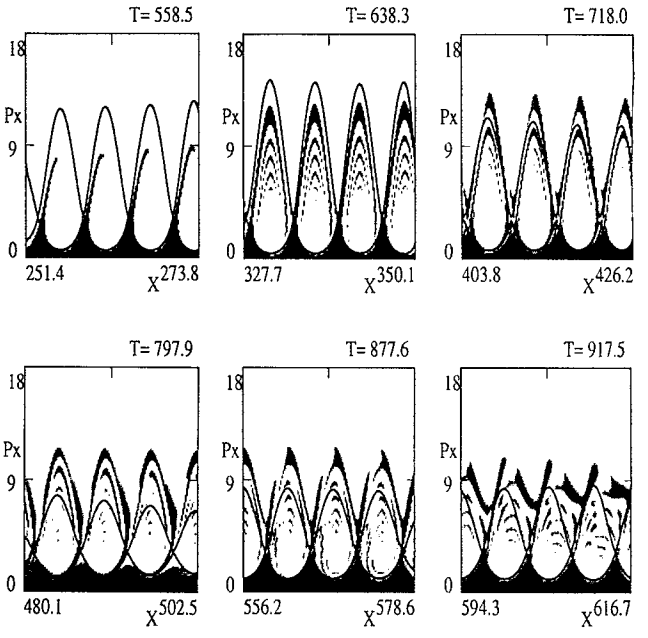

FIG. 12. Phase space window moving at $v_{\rm ph}$ shows the evolution of the fast electron generation in the LCP case. The solid line corresponds to the separatrix momentum of the marginally trapped electrons. The locations of the moving window are marked in Fig. 3.

regrowth. Therefore, the plasma wave collapses and is not able to trap electrons significantly anymore.

Figure 12 shows a window moving at the phase velocity of the LCP plasma wave. The spatial locations of the window at various times are shown in Fig. 3. The window provides snapshots of the particle acceleration process. As the strongest field region is reached, the electrons in the Gaussian wing become accelerated and their maximum energy approaches the value corresponding to the upper trapping limit. The fast particles escape the strong field region and thereafter become decoupled from the field, retaining their high energy.

As is evident from the simulations, the field–particle interaction is a transient phenomenon. A simple model that describes some of the basic features of the electron acceleration process is obtained by assuming the electric field

$$E(x,t)=Ee^{-x^2/w^2}\cos(kx-\omega t+\phi). \tag{41}$$

A Gaussian envelope is chosen for the sake of discussion. The electrons move initially at a velocity u_0 in the region $x\ll -w$. They are accelerated by the field (41) and acquire a final velocity u_∞ when $x\gg w$. The electrons are regarded as test particles, and therefore their reaction back onto the field is neglected.

The trajectory of the electron is obtained by integrating numerically the relativistic equation of motion. Figure 13 gives two typical examples of the trajectory, velocity, and kinetic energy of the electron as a function of time. The top graph represents a "low-field" case, where, in spite of the considerable velocity oscillations within the field region, the final speed u_∞ differs only marginally from u_0. In the

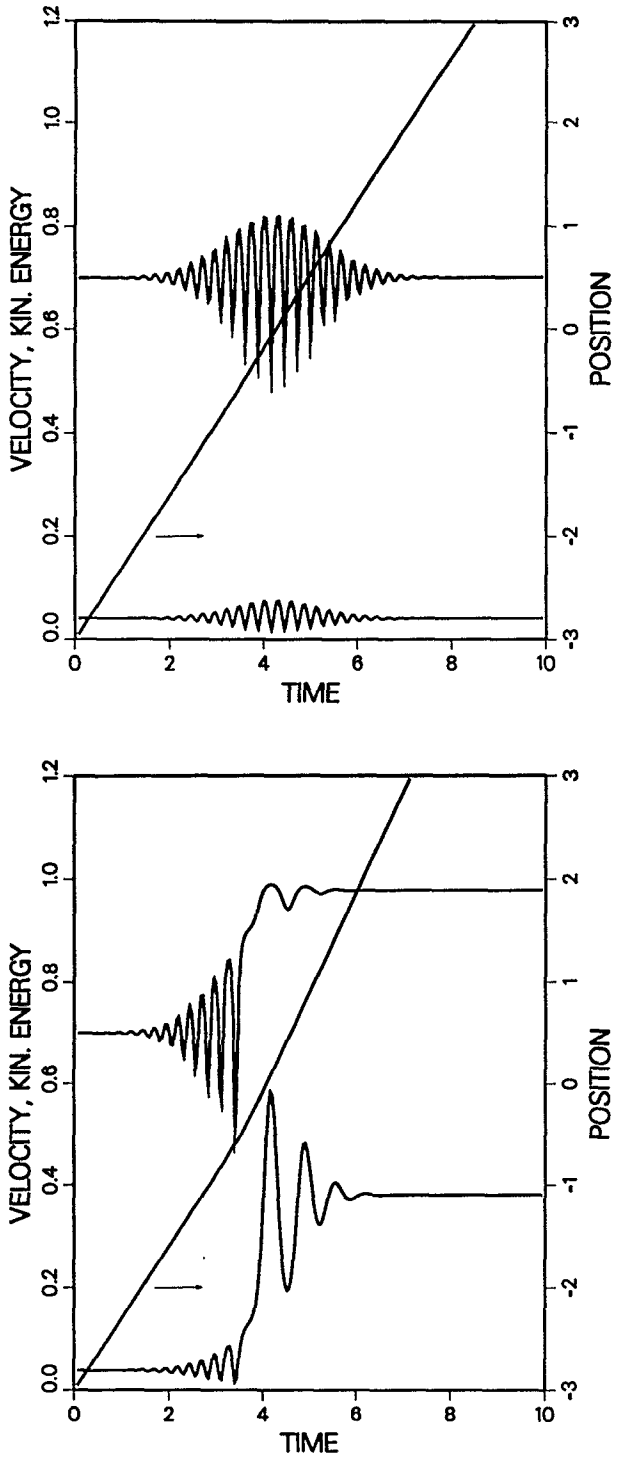

FIG. 13. The velocity v/c (upper wiggly curve), the kinetic energy $\gamma-1$ (scaled down by a factor $\frac{1}{10}$, lower wiggly curve), and the position x/w (use the right-hand scale) of a test particle versus time ct/w for two field strengths $eEw/mc^2=10$ (top figure) and $eEw/mc^2=20$ (lower figure). The initial velocity is $u_0/c=0.7$; the other parameters are $v_{ph}/c=0.9$, $w/\lambda=20$, and $\phi=0$.

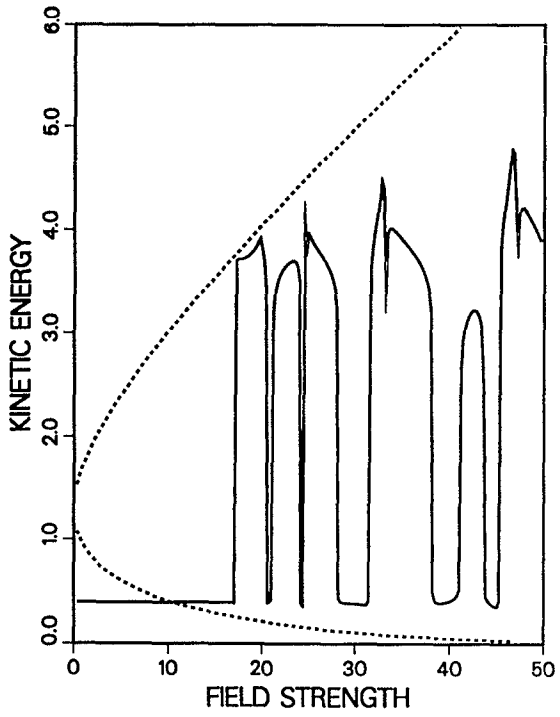

FIG. 14. The final kinetic energy W_∞/mc^2 of a test particle versus the field strength eEw/mc^2. Parameters are as in Fig. 13.

lower part, the total velocity change is large and thus efficient energy transfer takes place. In this "strong-field" case, the electrons get momentarily trapped. As the field is localized, the electrons can escape with a large energy increase before being rebounced by the out-of-phase part of the field. [For very slow ($v_{ph}\ll u_0$) intense fields there are also such trajectories where the electron gets trapped into the field or is rejected back to $x\to-\infty$, but these cases are irrelevant as regards the present paper.]

Figure 14 displays the final kinetic energy $W_\infty=mc^2[(1-u_\infty^2/c^2)^{-1/2}-1]$ of the electron versus the field strength E. An astounding feature is the abrupt change from no acceleration to full acceleration at $E=E_{cr}$. The transition point E_{cr} is practically unaffected by the field phase ϕ, if the field envelope is several wavelengths wide, i.e., $\kappa=kw\gg1$. The value of E_{cr} can be estimated from the relation

$$\frac{eE_{cr}}{mc^2k}=\xi\left[\frac{1-u_0v_{ph}/c^2}{(1-u_0^2/c^2)^{1/2}}-\left(1-\frac{v_{ph}^2}{c^2}\right)^{1/2}\right]. \tag{42}$$

For $\xi=1$ the above equation simply defines the field amplitude at which u_0 coincides with the lower trapping velocity $u_{low}=(v_{ph}-v_{tr})/(1-v_{ph}v_{tr}/c^2)$, where

$$v_{tr}/c=[1-(1+\eta)^{-2}]^{1/2}, \tag{43}$$

$$\eta=\frac{eE}{kmc^2(1-v_{ph}^2/c^2)^{1/2}}. \tag{44}$$

According to the numerical integrations one may use the value $\xi\approx2$ as a rule of thumb when $\kappa\gg1$.

For $E>E_{cr}$ the electron energy W_∞ jumps almost stepwise between zero and the maximum value

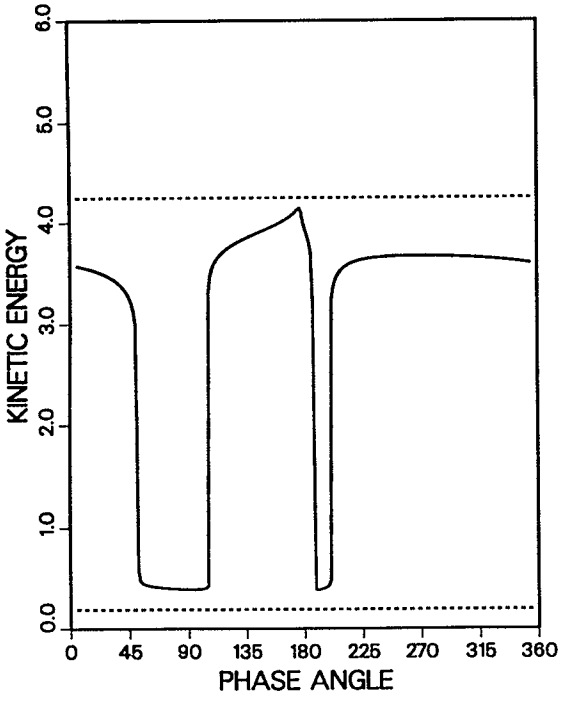

FIG. 15. The final kinetic energy W_∞/mc^2 of a test particle when the field phase ϕ is varied. The field strength is $eEw/mc^2=22$ and the other parameters are as in Fig. 13.

$$W_{\infty,\max}/mc^2=[1+\eta+(v_{\rm ph}/c)(2\eta+\eta^2)^{1/2}]\times(1-v_{\rm ph}^2/c^2)^{-1/2}-1, \quad (45)$$

where $E=E_{\rm cr}$ has to be used when evaluating η. Notice that $W_{\infty,\max}$ is the kinetic energy corresponding to the upper trapping velocity $u_{\rm up}=(v_{\rm ph}+v_{\rm tr})/(1+v_{\rm ph}v_{\rm tr}/c^2)$ at $E_{\rm cr}$, and it is thus independent of the field strength for $E>E_{\rm cr}$. The curve has an irregular structure with windows of field strength where no acceleration occurs at all.

If we fix the field amplitude E and vary its phase ϕ, which is equivalent to varying the initial position of the test electron, we obtain curves such as the one in Fig. 15. The characteristic feature is here, too, that the electron is not accelerated at all or gets almost a constant boost from the field. This behavior is most probably of the same origin as the stratified pattern appearing in Fig. 12.

It must be pointed out that the above analytical model has a limited validity range. The semiempirical relation (42), and consequently also (45), fails when u_0 deviates enough from $v_{\rm ph}$. For instance, in the case of Fig. 14 the value of $E_{\rm cr}$ obtained from the numerical integration agrees well with (42) down to $u_0\approx 0.6c$. For initial speeds in the range $u_0\leqslant 0.5c$, the particle acceleration seems to be fully absent. Furthermore, the maximum energy $W_{\max}$ shows significant variations with E, in particular, when the field region is only a few wavelengths wide (say, $\kappa<10$).

In the LCP (RCP) case of Table I, the analytical model predicts for $u_0>0.7c$ that the onset of efficient acceleration occurs at field strengths $eE_{\rm cr}/m\omega_p c\approx 0.43$ (0.22) or less. If the initial velocity u_0 is smaller, field strengths much larger than those occurring in the simulations are required. The final energy is according to (45) $W_{\infty,\max}/mc^2\approx 12$ (5).

If we add into the field (41) several Fourier components under the same envelope the acceleration behavior changes, but still some of the characteristic features are retained. For instance, the abrupt transition at $E_{\rm cr}$ survives, albeit the value of $E_{\rm cr}$ is reduced. At about 30% amplitude modulation with a spatial frequency $0.25k$, the lower acceleration limit in the LCP case decreases to $u_0\approx 0.5c$. The corresponding critical field decreases to $eE_{\rm cr}/m\omega_p c\approx 0.23$, if the total intensity is the same as in the single-mode case. The final particle energies drop to about $8mc^2$. In the RCP case, the changes are similar. Clearly the spectral broadening of the plasmon field facilitates the particle acceleration. A detailed study of this is, however, beyond the scope of this paper.

VI. SUMMARY AND DISCUSSION

We have investigated the stimulated Raman forward scattering in conditions relevant to the Raman and beat-wave current drive in reactor grade tokamak plasmas.[9,11] Our study includes relativistic Vlasov–Maxwell simulations and supporting envelope and test particle calculations. The emphasis of the study is in relativistic wave–particle interactions, which show many interesting features.

In the RCP simulation, an initially weakly damped plasma wave grows to a large amplitude and depletes the pump wave. Simultaneously, the plasma wave begins to interact with the electrons, which leads to a collapse of the plasma wave and to generation of fast electrons. In the LCP run, the wave–particle interaction and the fast electron generation seem to be more adiabatic and weaker, even though a hot tail of fast electrons has been included in the initial preparation. One reason for the difference is the second plasma wave that is created by the second Stokes scattering in the RCP simulation. The second plasma wave enhances the wave–particle interactions, because it has a smaller phase velocity than the plasma wave created in the first Stokes scattering. The k spectrum of the longitudinal field broadens considerably due to the appearance of the second Stokes coupling.

The simulations demonstrate the generation of ultrafast electrons in the Raman forward scattering. The observed maximum energies clearly exceed the estimate, based on the phase velocity of the plasma wave. A much better approximation for the maximum energy is obtained by using the upper trapping velocity as the characteristic velocity. In the trapping region of the plasma wave, a plateau forms because of the wave–particle interactions. In finer detail, there are striations in the distribution function that are similar to those obtained by using the simple model of Sec. V. A remarkable feature of the wave–particle interaction is its strength, despite the large difference between the electron thermal speed and the phase velocity of the wave. Even the lower trapping velocity $u_{\rm low}$ is in the simulations much larger than the thermal velocity.

In the RCP simulation, strong spatial modulations of the plasma wave amplitude are observed. The modulations and the nearly chaotic phase space behavior may be caused by the second plasma wave that is created in the second Stokes decay. The analysis of the short-wavelength modulations, however, calls for more advanced methods. An improvement would be the inclusion of the second spatial derivative into the envelope equation for the plasma wave, which would then resemble the nonlinear Schrödinger equation. The second Stokes scattering should also be included in order to describe the RCP system correctly. These improvements are, however, beyond the scope of this study.

Strong generation of the anti-Stokes wave is observed both in the RCP and LCP simulations. The estimated growth rates of SRS in the simulations are fairly close to the analytical estimates. At the intensity range considered, the effect of the anti-Stokes component on the SRS-F growth rate is small.

In the LCP run, the anti-Stokes scattering is important already at low frequencies of the pump wave. In the Vlasov simulation, the pump frequency in the LCP case was only $\omega_0=2.58\omega_p$, but the anti-Stokes scattering was not suppressed by the detuning. When the simulations were repeated by solving numerically the envelope equations, the mismatch was estimated from the linear dispersion relations and phase matching conditions. In the LCP case, the mismatch was rather small: $\delta_+=0.023\omega_p$. Strong anti-Stokes generation was observed also in the envelope calculation, in good agreement with the Vlasov simulation. The amplitudes of the plasma wave and of the Stokes wave were found to depend sensitively on the amount of the linear detuning of the anti-Stokes wave. The relativistic detuning of the plasma wave was found to be important only at very large amplitudes.

ACKNOWLEDGMENTS

The authors are indebted to the "Centre de Calcul Vectoriel pour la Recherche" (Ecole Polytechnique, Palaiseau, France) for computer time allocation on the Cray-2. P. B., A. G., and M. S. would like to acknowledge Professor Tudor W. Johnston and Professor Marc R. Feix for fruitful discussions and constant encouragements.

T. J. H. P. would like to thank the Finnish Cultural Foundation for financial support. This research was partly supported by the Finnish Ministry of Trade and Industry.

[1] N. J. Fisch, Rev. Mod. Phys. **59**, 175 (1987).
[2] C. S. Liu and M. N. Rosenbluth, Phys. Fluids **19**, 967 (1976).
[3] J. F. Drake, P. K. Kaw, Y. C. Lee, G. Schmidt, C. S. Liu, and M. N. Rosenbluth, Phys. Fluids **17**, 778 (1974).
[4] D. W. Forslund, J. M. Kindel, and E. L. Lindman, Phys. Fluids **18**, 1002 (1975).
[5] D. W. Forslund, J. M. Kindel, and E. L. Lindman, Phys. Rev. Lett. **30**, 739 (1973).
[6] K. Estabrook, W. L. Kruer, and B. F. Lasinski, Phys. Rev. Lett. **45**, 1399 (1980).
[7] K. Estabrook and W. L. Kruer, Phys. Fluids **26**, 1892 (1983).
[8] G. Bonnaud and C. Reisse, Nucl. Fusion **26**, 633 (1986).
[9] B. I. Cohen, R. H. Cohen, B. G. Logan, W. McCay Nevins, G. R. Smith, A. V. Kluge, and A. H. Kritz, Nucl. Fusion **28**, 1519 (1988).
[10] M. R. Amin and R. A. Cairns, Nucl. Fusion **30**, 327 (1990).
[11] S. J. Karttunen, T. J. H. Pättikangas, R. R. E. Salomaa, and S. K. Sipilä, Nucl. Fusion **31**, 1079 (1991).
[12] A. Ghizzo, P. Bertrand, M. M. Shoucri, T. W. Johnston, E. Fijalkow, M. R. Feix, and V. V. Demchenko, Nucl. Fusion **32**, 45 (1992).
[13] J. J. Thomson, Phys. Fluids **21**, 2082 (1978).
[14] D. W. Forslund, J. M. Kindel, W. B. Mori, C. Joshi, and J. M. Dawson, Phys. Rev. Lett. **54**, 558 (1985).
[15] G. Bonnaud, Plasma Phys. Controlled Fusion **29**, 573 (1987).
[16] K. Estabrook, W. L. Kruer, and M. G. Haines, Phys. Fluids B **1**, 1282 (1989).
[17] D. Pesme, S. J. Karttunen, R. R. E. Salomaa, G. Laval, and N. Silvestre, Laser Part. Beams **6**, 199 (1988).
[18] J. A. Heikkinen and S. J. Karttunen, Phys. Fluids **29**, 1291 (1986).
[19] B. I. Cohen, A. N. Kaufman, and K. M. Watson, Phys. Rev. Lett. **29**, 581 (1972).
[20] S. J. Karttunen and R. R. E. Salomaa, Phys. Rev. Lett. **56**, 604 (1986).
[21] A. Sjölund and L. Stenflo, Z. Phys. **204**, 211 (1967).
[22] H. Wilhelmsson, J. Plasma Phys. **3**, 215 (1969).
[23] A. Ghizzo, P. Bertrand, M. M. Shoucri, T. W. Johnston, E. Fijalkow, and M. R. Feix, J. Comput. Phys. **90**, 431 (1990).
[24] P. Bertrand, A. Ghizzo, T. W. Johnston, M. Shoucri, E. Fijalkow, and M. R. Feix, Phys. Fluids B **2**, 1028 (1990).
[25] T. Réveillé, P. Bertrand, A. Ghizzo, J. Lebas, T. W. Johnston, and M. Shoucri, Phys. Fluids B **4**, 2665 (1992).
[26] A. Ghizzo, P. Bertrand, J. Lebas, M. Shoucri, E. Fijalkow, and M. R. Feix, "Comparison between 1-D and $1\frac{1}{2}$-D Eulerian Vlasov codes for the numerical simulation of stimulated Raman scattering," to appear in J. Comput. Phys. (1992).
[27] R. J. Bickerton, J. W. Connor, and J. B. Taylor, Nature Phys. Sci. **229**, 110 (1971).
[28] M. J. Alava and S. J. Karttunen, Plasma Phys. Controlled Fusion **32**, 1135 (1990).
[29] M. N. Rosenbluth and C. S. Liu, Phys. Rev. Lett. **29**, 701 (1972).
[30] S. J. Karttunen and R. R. E. Salomaa, IEEE Trans. Plasma Sci. **PS-15**, 134 (1987).